communications biology

A Nature Portfolio journal

Article

https://doi.org/10.1038/s42003-025-08103-x

Molecular basis of TRPV3 channel blockade by intracellular polyamines

Jingying Zhang[1,2], Peng Yuan[1,2], Colin G. Nichols[3,4] & Grigory Maksaev[3,4]

ThermoTRPV1-4 channels are involved in the regulation of multiple physiological processes, including thermo- and pain perception, thermoregulation, itch, and nociception and therefore tight control of their activity is a critical requirement for correct perception of noxious stimuli and pain. We previously reported a voltage-dependent inhibition of TRPV1-4 channels by intracellular polyamines that could be explained by high affinity spermine binding in, and passage through, the permeation path. Here, using electrophysiology and cryo-electron microscopy, we elucidate molecular details of TRPV3 blockade by endogenous spermine and its analog NASPM. We identify a high-affinity polyamine interaction site at the intracellular side of the pore, formed by residues E679 and E682, with no significant contribution of residues at the channel selectivity filter. A cryo-EM structure of TRPV3 in the presence of NASPM reveals conformational changes coupled to polyamine blockade. Paradoxically, although the TRPV3 'gating switch' is in the 'activated' configuration, the pore is closed at both gates. A modified blocking model, in which spermine interacts with the cytoplasmic entrance to the channel, from which spermine may permeate, or cause closure of the channel, provides a unifying explanation for electrophysiological and structural data and furnishes the essential background for further exploitation of this regulatory process.

The natural organic cations polyamines (PAs: putrescine, spermidine, and spermine) are present in sub-millimolar concentrations in cellular cytoplasm[1], and sometimes at much higher concentrations in extracellular fluids[2]. Due to their high positive charge, PAs have long been recognized as protein expression regulators via binding to DNA and RNA molecules[3] and are involved in cell growth and proliferation[4,5], inflammation and immune response[6–8], parasite and viral infections[9,10], and plant responses to abiotic stress[11]. Since PAs exist mostly in bound forms, their intracellular free concentration is estimated to be ~10–100 μM. Intracellular PA levels are normally stable, but they decrease with age, and significant changes are linked to neuronal degeneration and brain aging[12–15], various types of cancer[16–18], and some rare developmental diseases[19,20]. PA-targeted treatment has proven effective for maintenance of cognitive functions[21–23], gastrointestinal balance[24,25], Bachman-Bupp syndrome[19], and for cancer management[26–29]. PAs are also known as strong modulators of cation channels of different nature, such as inward-rectifier potassium channels (Kir channels)[30–32], BK channels[33], voltage-gated sodium channels[34], ionotropic glutamate receptors[35,36], cyclic nucleotide-gated channels (CNGs)[37,38], and at least several members of the canonical[39,40], melastatin[41,42], and vanilloid TRP subfamilies[43,44]. A certain degree of PA permeability has also been reported or hypothesized for some channels, including CNG[37], TRPV1[44], and TRPV2[45].

The TRPV protein subfamily generates two groups of structurally related cationic channels: TRPV1–4 that are essentially non-selective, and TRPV5-6 that are highly Ca^{2+}-selective. TRPV1-4 channels are gated by various stimuli: natural compounds (such as capsaicin and cannabinoids), endogenous ligands, pH, as well as synthetic drugs and heat[46]. Gating of these channels is not strongly voltage-independent, except for TRPV1[47,48]. Broad expression of TRPV1-4 channels in multiple organs and tissues reflects their involvement in many physiological processes. Of particular interest is expression of TRPV1-4 in excitable cells (such as neurons and pancreatic β-cells, in which at least TRPV1, 2, and 4 are functionally expressed and modulate excitation), and in dividing, proliferating, and cancer cells that are characterized by both strongly depolarized membranes and elevated PA levels. TRPV dysfunction results in a wide range of pathologies, including chronic pain and hyperalgesia (TRPV1, 4), itch, pruritus, and skin Olmsted syndrome (TRPV3), arthritis and other musculoskeletal and neurological diseases (TRPV4), as well as various immune system–related disorders (TRPV2). Since the most severe pathologies are typically related to channel over-

[1]Department of Pharmacological Sciences, Icahn School of Medicine at Mount Sinai, New York, NY, USA. [2]Department of Neuroscience, Icahn School of Medicine at Mount Sinai, New York, NY, USA. [3]Department of Cell Biology and Physiology, Washington University School of Medicine, St. Louis, MO, USA. [4]Center for Investigation of Membrane Excitability Diseases, Washington University School of Medicine, St. Louis, MO, USA. e-mail: gmaksaev@wustl.edu

activity[49], inhibition of these channels may serve as a powerful tool for treatment of multiple TRPV-related diseases. Therefore, pharmacology of TRPV channels requires investigation of novel regulatory pathways, one of which is our recently reported inhibition of TRPV channels by endogenous intracellular polyamines[43]. PA inhibition of TRPV1-4 is strongly voltage-dependent, peaks around 0 mV, and is most potent for TRPV3. Similar (although not identical) voltage-dependent block by spermine in different TRPV channels suggests a common molecular mechanism. Here, using combined electrophysiological and cryo-EM approaches, we reveal the molecular determinants of PA inhibition of TRPV3 channels.

Results

TRPV channel inner pore structure and electrostatics

The strong voltage-dependence of TRPV channel block by intracellular spermine[43] naively suggests that spermine interacts with a site located within the membrane field, i.e. inside the conductive pore. The pore inner cavity-lining transmembrane helix 6 (S6) does not contain any charged amino acids (Fig. 1A), in contrast to inward rectifier potassium channels, which require negative charge within the inner cavity for strongly voltage-dependent block by spermine[30,50,51]. Alternatively, spermine may interact with negative charges that are located below the inner cavity, at the C-terminal negatively charged region, or that are located above the inner cavity, within the selectivity filter (SF). These two pore regions are structurally most different between TRPV3, and TRPV1 and 4 (Fig. 1A), and we therefore hypothesized that these two regions (SF and intracellular negatively charged 'ring' (Fig. 1)), may be key players in spermine interaction, and potentially underlie the difference in potency between TRPV sub-types.

Role of the selectivity filter in TRPV3 inhibition by intracellular PA

Voltage-dependent inhibition by intracellular spermine is stronger in TRPV3 channels than in TRPV1 and TRPV4[43], and parallels difference in the classic SF 'GXGD' motif, where X = Met for TRPV1 and TRPV4, but X = Leu in TRPV3 (Fig. 1A). To address whether the SF plays any significant role in intracellular PA inhibition of TRPVs, we first introduced a single mutation L639M into the TRPV3 SF to mimic the amino acid sequence in TRPV1 and TRPV4 SFs (Figs. 1, 2). In excised-membrane patches, a stepped voltage protocol[43] revealed no significant differences in the effect of 100 μM intracellular spermine on this mutant versus the wild type (Fig. 2G, Table S1). In TRPV1, 3 and 4 channels a conserved negatively charged aspartate residue (D641 in TRPV3) located 2 residues beyond L639 (Fig. 1) plays a role in activation and potentiation of the channel by extracellular gadolinium ions[52] and spermine[44]. In TRPV3, the D641 residue is also involved in inhibition by extracellular acid[53], Gd^{3+}[52], and Mg^{2+}[54]. However, similarly to the L639M mutant, we observed only marginal effect of the TRPV3 D641N mutation on 100 μM intracellular spermine inhibition (Fig. 2B, G, Table S1). Taken together, these results indicate minimal involvement of the SF in TRPV channel inhibition by intracellular PA.

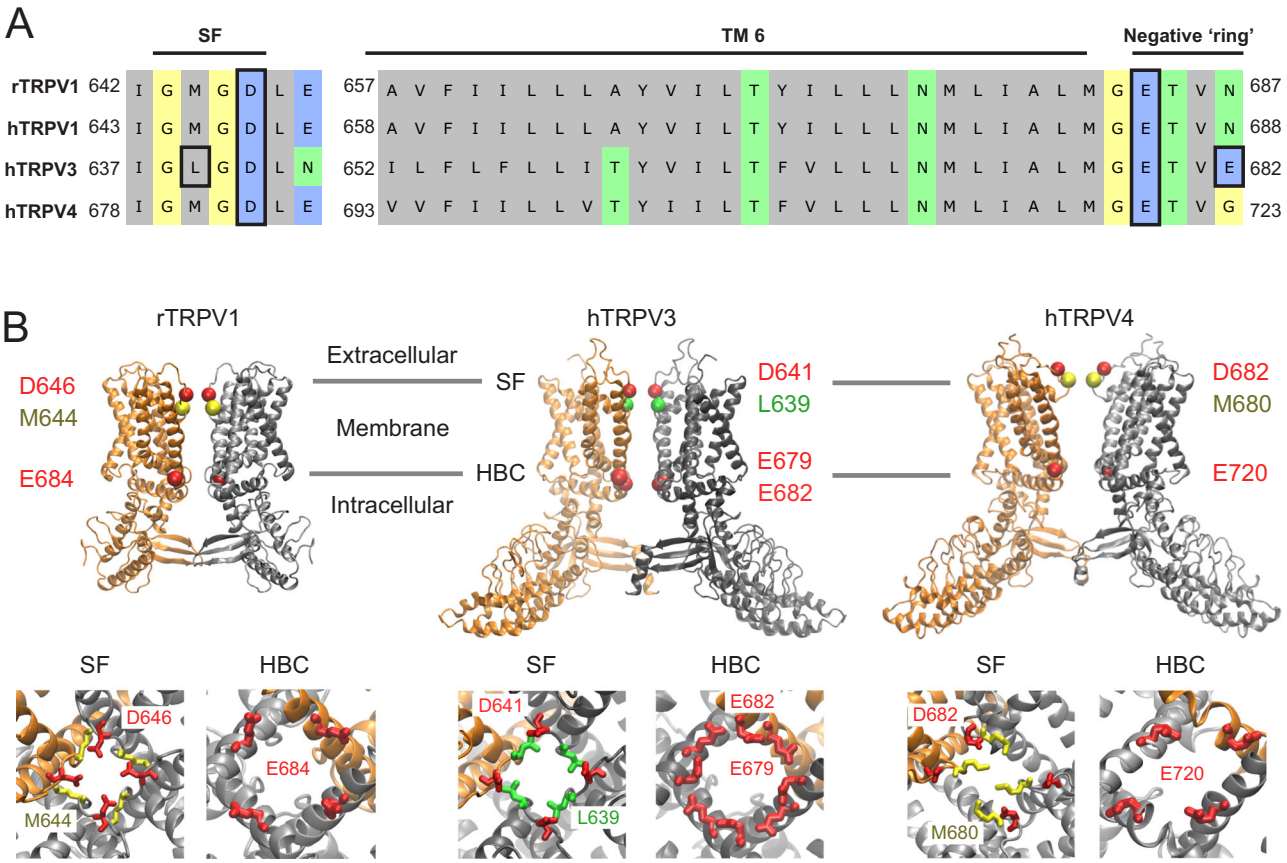

Fig. 1 | Conductive pores of TRPV channels. (**A**) Amino acid sequences in the pore and inner cavity regions of TRPV channels. The mostly hydrophobic inner cavity-lining S6 is flanked by a charged SF extracellular loop and C-terminal regions. Two unconserved residues in TRPV3 – L639 (in SF) and E682 as well as highly conserved negatively charged residues in SF and in C-terminal negatively charged 'ring' are highlighted with black boxes. (**B**) Potential polyamine interaction sites. Top row: open structures of rat TRPV1 (PDB: 7L2M), human TRPV3 (PDB: 8V6N), and human TRPV4 (PDB: 8T1D). Only two opposing monomers are shown for clarity. Two hypothesized interaction site at the SF (labeled red for acid residues and yellow for methionine in TRPV1 and TRPV4 or green for leucine in TRPV3) and the C-terminal negatively charged 'ring' at the HBC (labeled red for glutamic acid) are highlighted. Bottom row: Close up views of these regions are shown for each channel viewed from the cytoplasm through the membrane plane.

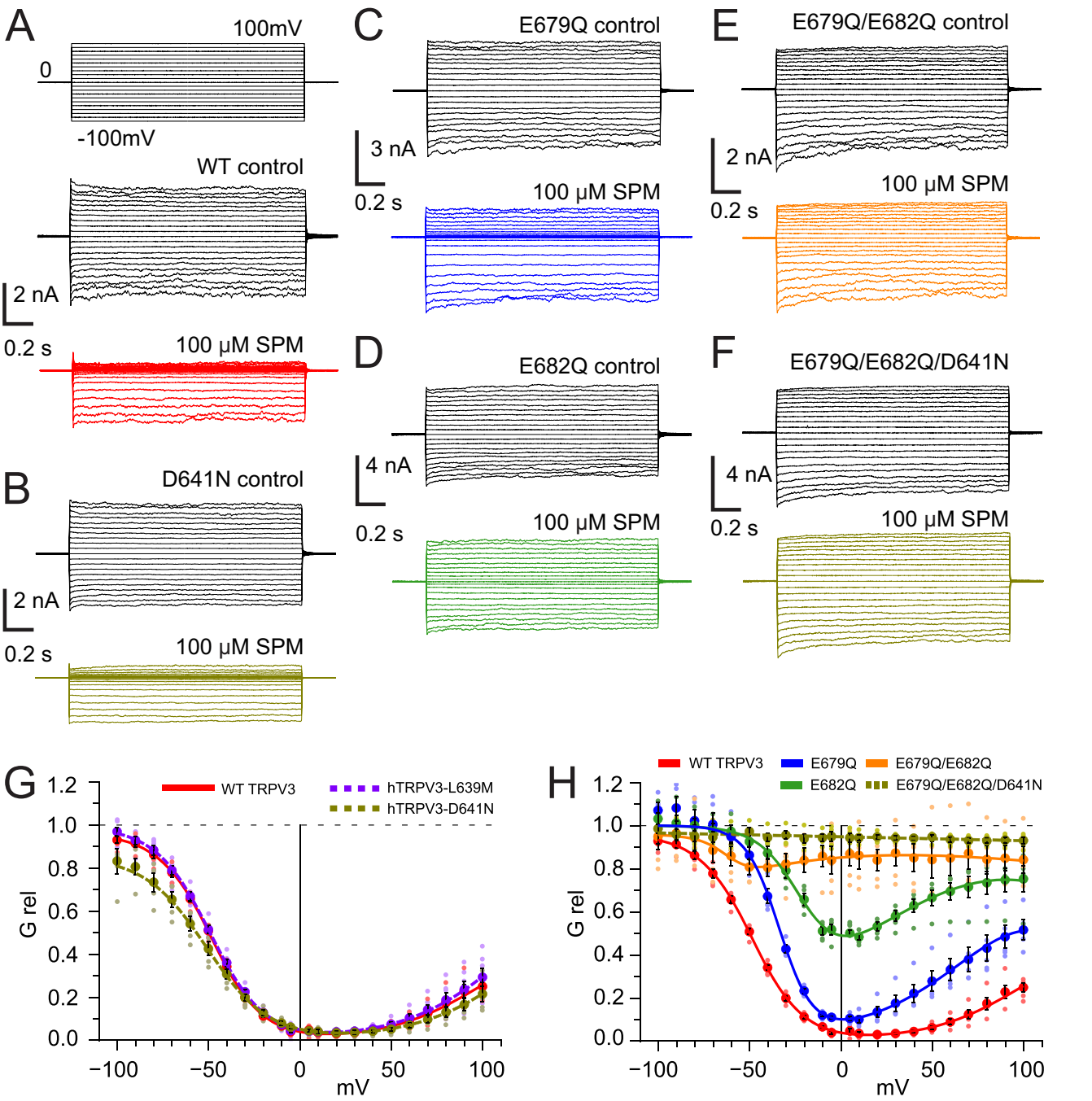

Fig. 2 | Spermine block of WT and mutant hTRPV3 channels. A–F Representative traces of the 2-APB-induced hTRPV3 currents (WT and indicated mutants), measured using a voltage-step protocol (A, top) in absence (black traces, controls) and presence (color-coded traces) of 100 μM cytoplasmic spermine. **G** Averaged ($n = 6$ for WT, $n = 7$ for L639M, $n = 5$ for D641N, ± SE) G_{rel}-V relationships for WT hTRPV3 (solid red line) and selectivity filter L639M (dashed violet line) and D641N (dashed dark yellow line) mutants in the presence of 100 μM cytoplasmic spermine. **H** Averaged ($n = 6$ for WT, $n = 5$ for all mutants, ± SE) G_{rel}-V relationships for WT hTRPV3 (red line), single E679Q mutant (blue line), single E682Q mutant (green line), double E679Q/E682Q mutant (orange line), and triple E679Q/E682Q/D641N mutant (dashed dark yellow line) in presence of 100 μM cytoplasmic spermine. Datasets were fitted with the sum of two Boltzmann distributions except E679Q/E682Q/D641N mutant, which was fitted with a linear regression. WT TRPV3 data is taken from ref. 43.

Negatively charged 'ring' defines TRPV3 inhibition by intracellular PA

In mouse TRPV3, negatively charged E679 and E682, located at the cytoplasmic entrance to the inner cavity, are responsible for tonic inhibition of the channel by intracellular Mg^{2+}[54]. We used available open cryo-EM structures to examine this location in rat TRPV1, human TRPV3, and human TRPV4 (Fig. 1B). In TRPV3, E679 and E682 are both in close proximity to the pore lumen, forming a negatively charged 'ring' (Fig. 1) immediately below the pore constriction formed by I674 residues at the helical bundle crossing (HBC). Interestingly, TRPV1 and TRPV4 have only one negatively charged residue each (E684 and E720, respectively, Fig. 1A, B) at this location, and lower charge density. Spermine interaction with this ring would be predicted to be strongest in TRPV3, correlating with the significantly stronger effect of intracellular spermine on TRPV3 compared to TRPV1 and 4[43], and consistent with experimental data suggesting that PA inhibition of BK potassium channels involves interaction at the analogous location[33].

We generated two single point mutations (E679Q, E682Q), as well as double mutation E679Q/E682Q and measured channel activity using the

Table 1 | Results of fitting of the G_{rel}-V relationships for WT TRPV3 (Fig. 2H), its mutants, WT TRPV1, and WT TRPV4 with the sum of two Boltzmann distributions (Function 1) for inhibition by 100 μM intracellular spermine

	WT TRPV3[a]	TRPV3-E679Q	TRPV3-E682Q	TRPV3-E679Q/E682Q	WT TRPV1[a]	WT TRPV4[a]
V^{mid}_1, mV	−48.9	−33.8	−21.6	−44.2	−22.9	−26.1
Z_1, e	−1.81	−2.70	−1.83	−1.54	−3.28	−4.07
V^{mid}_2, mV	82.5	60.0	7.6	−36.3	17.1	9.7
Z_2, e	−1.27	−0.87	−1.14	−1.86	−1.99	−1.56
Net charge at the 'ring' position	−8	−4	−4	0	−4	−4

[a]Data for WT TRPV1, WT TRPV3, and WT TRPV4 block by 100 μM spermine were taken from[43].

same voltage step protocol[43] in the presence of 100 μM intracellular spermine (Fig. 2). In excised patches, spermine inhibition of E679Q was moderately relieved compared to WT (Fig. 2C, H). Spermine inhibition was strongly relieved in E682Q (Fig. 2D, H), and was essentially abolished in double E679Q/E682Q mutant channels (Fig. 2E, H). Fitting of G_{rel}-V curves with the sum of two Boltzmann distributions (*Function 1*, Fig. 2H and Table 1) indicated only moderate changes of both gating charges and the position of V^{mid}_1 (descending distribution, blocking) in all three mutants compared to WT, but a strong shift of V^{mid}_2 (ascending distribution, unblocking) to hyperpolarizing potentials, reflecting increasingly potent relief of block with decreasing net charge of the negatively charged 'ring'. G_{rel}-V curves were well predicted by the 2-state blocking model (*Function 2)*, by assuming that these mutations had additive effects on reduced potency of block (k_a, k_b) and, most dramatically, by increasing the permeation constant (K_P), without affecting the voltage dependence of any transition (reviewed in more detail in *Discussion*). While neutralization of the external aspartate (in the D641N mutant) had no overall significant effect on its own (Fig. 2G, Table S1), neutralization of all pore-lining charges in the triple TRPV3-D641N/E679Q/E682Q mutant completely abolished the inhibiting effect of intracellular spermine (Fig. 2F, H). Together, these results indicate a critical role of residues E679 and E682 in the negatively charged 'ring' at the cytoplasmic entrance to the pore in interacting with blocking polyamines, and a minor role of the extracellular D641.

Gain-of-function mutant K169A

Although open conformation structures of TRPV3 in complex with its agonists 2-APB and THCV have been obtained recently[55], TRPV3 activity appears to decay in the continuous presence of the agonist 2-APB[56]. However, a TRPV3 gain-of-function mutant K169A[57,58], which activates spontaneously in excised patches, does not significantly inactivate, and adopts an essentially open conformation in the presence or absence of agonists[56]. In excised patches, spontaneously active TRPV3-K169A in the absence of agonist was still inhibited by intracellular spermine in the same voltage-dependent manner and with similar efficacy as WT (Fig. 3A). Moreover, the double E679Q/E682Q mutation, introduced into the K169A background, resulted in a virtually identical pattern of spermine inhibition relief (Fig. 3A).

Thus, both WT and K169A share the same PA blocking mechanism and, since K169A does not inactivate, this mutant may be conformationally stable enough to capture polyamine-inhibited structures. NASPM, a bulky synthetic spermine analog (Fig. 3D), is an efficient blocker of Ca^{2+}-permeable AMPA receptors[35,36], and NASPM binding within the inner cavity of AMPA receptors has been identified by cryo-electron microscopy (cryo-EM)[59]. As we showed previously, intracellular NASPM blocks WT TRPV3 channels with similar voltage-dependence to spermine, albeit with much weaker permeation[43]. But, unlike spermine, NASPM also induces a potent voltage-independent inhibition at even low NASPM concentrations[43]. As shown in Fig. 3B, spontaneously active K169A also showed strongly voltage-dependent inhibition by intracellular NASPM but, in contrast to WT, K169A did not demonstrate any additional voltage-independent inhibition in the presence of 100 μM intracellular NASPM. Voltage-dependent NASPM inhibition of K169A had similar concentration dependence to WT[43], showing signs of channel permeation at positive potentials and block relief (Fig. 3B and Table S2). Inhibition was virtually absent at −70 mV within 1 – 100 μM NASPM range, while the estimated NASPM IC_{50} at 0 mV was about 15 μM (Fig. 3B).

To confirm the involvement of the negatively charged 'ring' in NASPM inhibition, we further introduced the same mutations tested previously in WT TRPV3, into the TRPV3-K169A background. Again, similarly to WT, we observed relief of NASPM block by either E679Q or E682Q single mutants, with no change in the steepness of the voltage dependence, and with no evidence of permeation (Fig. 3C). The double E679Q/E682Q mutation further weakened NASPM block on this K169A background and now showed significant NASPM permeability at 100 μM and almost complete block relief at 10 μM (Fig. 3C). Fitting of the TRPV3-K169A mutant data with a sum of two Boltzmann distributions (*Function 1*, Fig. 3C, Table 2) demonstrated qualitative similarity between behavior of the same mutants in the WT TRPV3 background subject to spermine block and in the TRPV3-K169A background subject to NASPM block. Again, G_{rel}-V curves were reasonably well predicted by the 2-state blocking model (*Function 2*), by assuming only that these mutations had additive effects on reduced potency of block (k_a, k_b) and by increasing the permeation constant (K_P), without affecting the voltage dependence of any transition (Fig. 6D and Table 3), confirming the similar role of E679/E682 residues in both WT TRPV block by spermine and TRPV3-K169A block by NASPM.

Structure of human TRPV3 in the presence of NASPM

Together with the bigger size of NASPM (compared to spermine), the above results suggest the TRPV3-K169A + NASPM pair as a system of choice for structural investigation of the mechanism of TRPV polyamine block, and hence we aimed at visualization of NASPM interaction with spontaneously open and non-inactivating TRPV3-K169A mutant channels using cryo-EM. We determined the cryo-EM structure of full-length human TRPV3-K169A in nanodiscs, in the presence of 100 μM NASPM, to an overall resolution of 3.39 Å with *C4* symmetry imposed (Fig. S1 and Table 4), which is on par with available TRPV3 cryo-EM structures[60–63]. The cryo-EM density map allowed us to build an atomic model that included residues 117 to 748.

The structure of human TRPV3-K169A in the presence of NASPM was similar to previously published domain-swapped four-fold symmetric tetrameric structures of ligand-free WT and K169A mutant[56,58,64], with each monomer consisting of extensive N- and C-termini, a transmembrane domain formed by six transmembrane helices, and the TRP helix (Fig. 4A, B). Multiple lipid-like densities were found surrounding the channel (Fig. 4A, B, labeled in yellow). The spatial organization and orientation of lipid densities were very similar to those previously reported for the open ligand-free conformation of human TRPV3-K169A (PDB: 6UW6)[56] and open agonist-bound human WT TRPV3 (PDB: 8V6L, 8V6N)[55]. Although two distinct conformations, open (69%) and inactive (31%), were determined for the ligand-free K169A mutant[56], this mutant channel adopted only a single conformation in the presence of NASPM (Fig. 4, S1) with higher overall similarity to the open K169A conformation (Fig. 4D, RMSD = 0.96 Å and 2.65 Å vs open and closed structures respectively). Significant differences compared to the apo closed state were

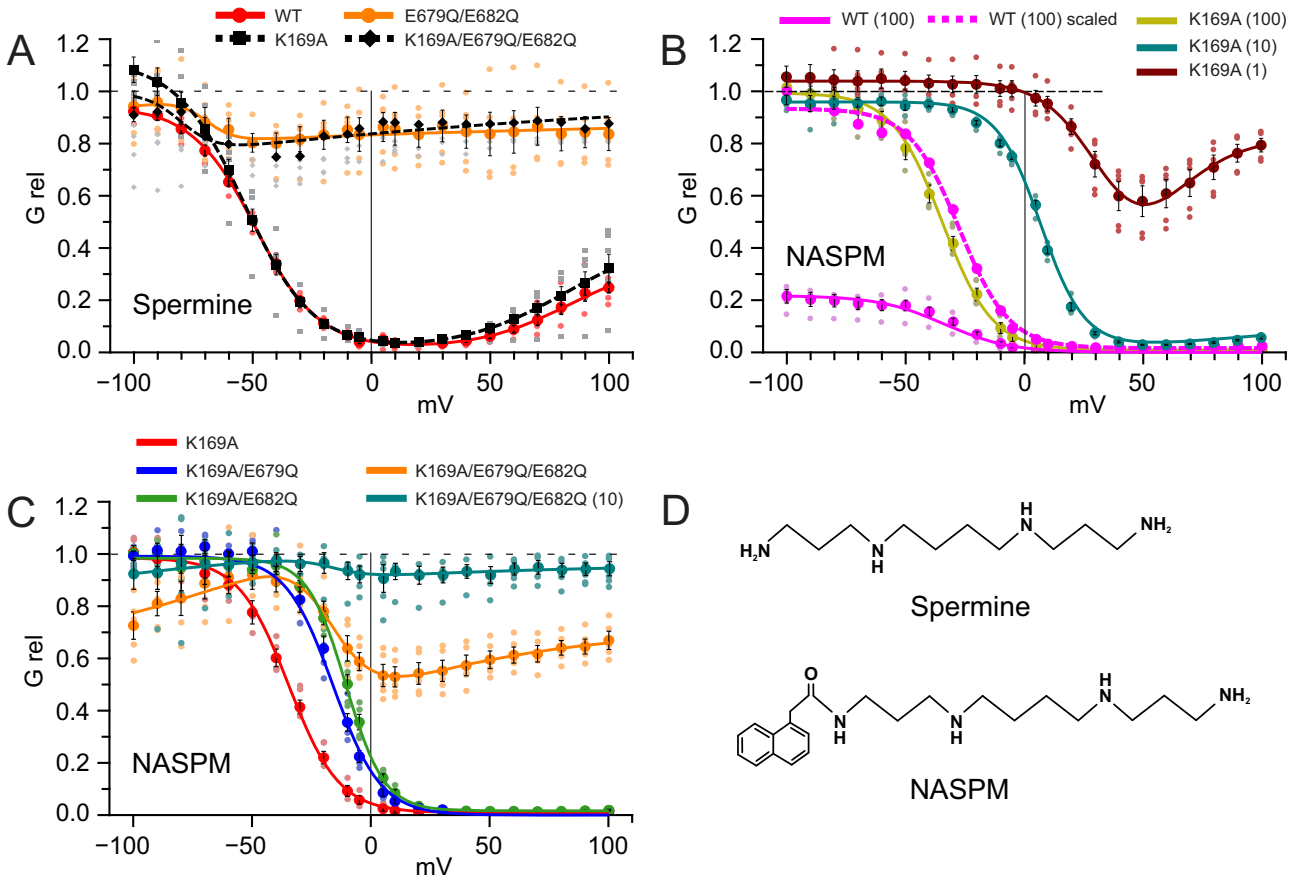

Fig. 3 | Blocking of hTRPV3-K169A by polyamines. A Averaged (n = 6 for WT, n = 7 for K169A, n = 5 for E679Q/E682Q, n = 5 for K169A/E679Q/E682Q, ± SE) G_{rel}-V relationships for WT TRPV3 (solid red line), TRPV3-K169A (dashed red line), TRPV3-E679Q/E682Q (solid orange line), and TRPV3-K169A/E679Q/E682Q (dashed orange line) in presence of 100 μM intracellular spermine. **B** Averaged (n = 5 for all, ± SE) G_{rel}-V relationships for WT TRPV3 (solid pink line), normalized WT TRPV3 (dashed pink line), and TRPV3-K169A (solid yellow line), in the presence of 100 μM intracellular NASPM, and TRPV3-K169A in the presence of 10 μM (teal line) and 1 μM (brown line) intracellular NASPM. Similarity of K169A and normalized WT G_{rel}-V relationships suggests voltage-independent inactivation mode of WT TRPV3 in the presence of NASPM, which is absent for K169A mutant. Datasets were fitted with Boltzmann distributions (Function 1). Unscaled WT TRPV3 data is taken from ref. 43. **C** Averaged (n = 5 for all, ± SE) G_{rel}-V relationships for TRPV3-K169A (solid red line), TRPV3-K169A-E679Q (solid blue line), TRPV3-K169A-E682Q, and TRPV3-K169A (solid orange line), in the presence of 100 μM intracellular NASPM, as well as TRPV3-K169A in presence of 10 μM intracellular NASPM (teal line). Datasets were fitted with Boltzmann distributions (Function 1), fitting results are presented in Table S2. (**D**) Molecular structures of spermine and NASPM, respectively.

localized to the distal C-terminal domain, where the CTD gating 'switch'[56,58] was found in an 'activated' α-helical conformation, and to the N-terminal domain, with the finger 5 loop from the adjacent ankyrin repeat domain (ARD) slightly rotated (Fig. 4C). A nearly identical 'activated' α-helical conformation of the CTD gating 'switch' was also reported for open agonist-bound human WT TRPV3[55], which suggests no influence of the K169A mutation on the behavior of the gating 'switch'. While these features of the N- and C-termini indicate overall similarity to the previously reported open and inactivated (PDB: 6UW9) conformations of K169A TRPV3[56], the pore-lining S6 helix clearly maintained a π-helical structure at the HBC constriction (formed by the I674 residue side chains, Fig. 4E), as in the open and closed conformations, in contrast to an α-helix in the inactivated agonist-bound state in nanodiscs[56]. Thus, despite the 'activated' CTD gating 'switch' and displaced ARD finger 5 loop, the overall structure of the conductive pore itself was quite similar to the closed channel pore, as described in detail below.

Table 2 | Results of fitting of the G_{rel}-V relationships for TRPV3-K169A mutants with one (K169A, K169A/E679Q, K169A/E682Q), or the sum of two (K169A/E679Q/E682Q), Boltzmann distributions (Function 1) for inhibition by 100 μM intracellular NASPM (Fig. 3C)

	K169A	K169A/E679Q	K169A/E682Q	K169A/E679Q/E682Q
V^{mid}_1, mV	−34.7	−16.0	−10.7	−16.5
Z_1, e	−2.38	−2.52	−3.13	−2.81
V^{mid}_2, mV				−36.6
Z_2, e				−0.48
Net charge at the 'ring' position	−8	−4	−4	0

TRPV3 ion conduction pore in the presence of NASPM

While the high quality of the cryo-EM density map was sufficient to resolve annular and inter-subunit lipid densities (Fig. 4A, B), no NASPM-attributable density was detected either inside or outside of the conductive pore. To address potential asymmetry induced by NASPM or partial occupancy of bound NASPM, we also determined the structure without imposed symmetry. The structure was essentially identical to that with C4 symmetry (Fig. S2), and still showed no density corresponding to bound NASPM. Despite the CTD gating 'switch' α-helical 'activated' conformation (Fig. 4C), the TRPV3-K169A mutant pore was essentially closed at both the lower (HBC at I674) and upper (SF at G638) gates (Fig. 5) with similar inner

Table 3 | Optimized parameters used in Fig. 6C, D

	Spermine (100 μM)				NASPM (100 μM)			
Parameter	WT	E679Q	E682Q	E67Q-E682Q	K169A	K169A-E679Q	K169A-E682Q	K169A-E679Q-E682Q
K_a^1	3	2	0.5	0.2	0.3	0.1	0.09	0.06
Z_1*	1	1	1	1	1	1	1	1
K_a^{-1}	25	50	60	70	4.00	4.75	5.75	6.00
Z_{-1}*	−1	−1	−1	−1	−1	−1	−1	−1
K_a^2	35	80	110	400	0.055	0.075	0.4	11
Z_2*	1.6	1.6	1.6	1.6	1.2	1.2	1.2	1.2
K_C*	6	6	6	6	2	2	2	2
Z_C*	0	0	0	0	0	0	0	0
$K_P = K_a^2 / K_a^{-1}$	1.4	1.6	1.8	5.7	$1.4*10^{-2}$	$1.6*10^{-2}$	$7*10^{-2}$	1.8

Parameters labeled with an asterisk (*) were fixed.
Transitions to and from the closed state were considered voltage-independent (i.e. net charge $Z_C \equiv 0$).

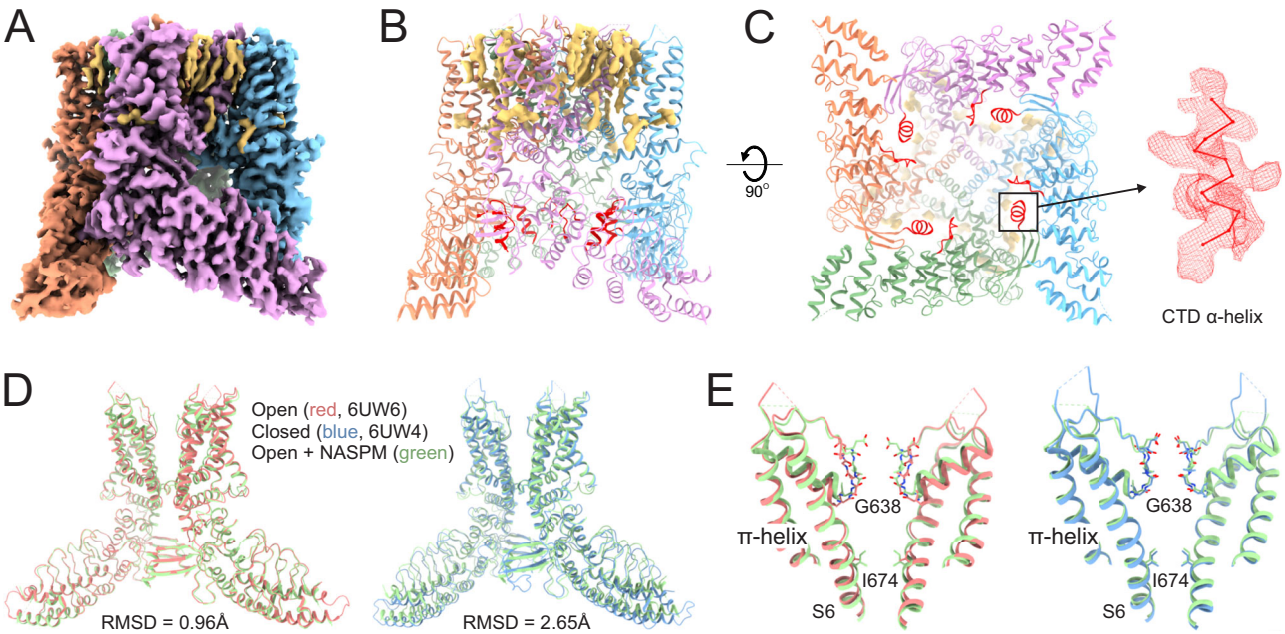

Fig. 4 | Cryo-EM structure of TRPV3-K169A in nanodiscs with NASPM. A Cryo-EM density map. Subunits are uniquely colored and lipid-like densities are colored in yellow. **B** Side view of the modeled TRPV3-K169A structure. Electron density of the distal C-terminal domain and finger 5 of ARD are labeled in red. **C** Bottom view of (**B**). C-terminal 'gating switch' (arrow) adopts clearly an α-helical conformation, as in open conformation of the channel. Superposition of the overall structure (**D**) and the pore region (**E**) of TRPV3-K169A + NASPM (green) with TRPV3-K169A open (PDB: 6UW6, red) and WT TRPV3 closed (PDB: 6UW4, blue) structures. RMSD values for TRPV4-K169A + NASPM vs open (6UW6) and closed (6UW4) structures are presented in (**D**). Constrictions at SF (G638) and HBC (I674), as well as the π-helical bulge in S6 helix are labeled in (**E**). Only two opposing subunits are shown for clarity in (**D**, **E**).

cavity shape to the closed WT channel (Fig. 5C), and with similar constriction dimensions: 5.96 Å vs 5.34 Å at the lower (HBC, I674) gate and 5.26 Å vs 4.48 Å at the upper (SF, G638) gate (Fig. 5B), opposed to 9.4 Å and 7.4 Å (PDB: 8V6N) of the open state. There was ~2 Å local expansion of the outer mouth of the pore right above the SF (Fig. 5C) in the immediate vicinity of extracellular residue D641. Unfortunately, in the predicted region of spermine interaction, the quality of the local cryo-EM density map was insufficient to unambiguously identify the orientation of E679 and E682 side chains (Fig. S1D, inset), although the TM backbones clearly adopted closed conformations in this region (Fig. 5A, C).

Discussion

We recently demonstrated a similarly voltage- and concentration-dependent blocking effect of intracellular spermine on TRPV channels, most potently on TRPV3[43], in each case with voltage-dependent relief of block at positive potentials. A previously proposed model for similarly weakly PA-permeable CNG channels[37,38] adequately described spermine block using high- and low-affinity PA binding sites, with relief of block resulting from PA permeation[43]. In the present study, we used a combination of mutagenic and structural approaches to identify the molecular determinants of PA block in TRPV3 channels.

Consistent with the main PA interaction site being below the HBC at the negatively charged 'ring' formed by the E679 and E682 residues (Fig. 1), neutralization of either of the two ring glutamates in TRPV3-E679Q or E682Q single mutants significantly decreased spermine block efficiency, while removal of both residues in the double E679Q/E682Q mutant resulted in almost complete relief of block across the whole range of membrane potentials (Fig. 2H). Fitting of G_{rel}-V curves with the sum of two Boltzmann distributions (Fig. 2H, Table 1) indicated a strong shift of $V^{mid}{}_2$ to hyperpolarizing potentials as the primary driver of weaker spermine block in TRPV3 mutants and model predictions are consistent with decrease of the net negative charge in the 'ring' leading to a reduced blocking affinity,

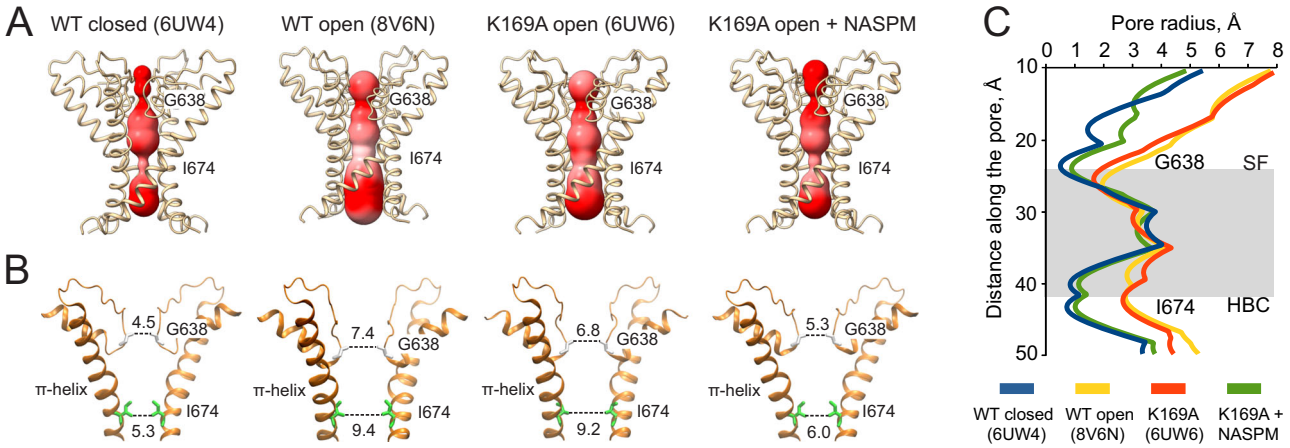

Fig. 5 | Structure of the conductive pore of TRPV3-K169A in the presence of NASPM. A The pores of human TRPV3 in the absence of agonists (PDB: 6UW4) and in the presence of 2-APB (PDB: 8V6N), TRPV3-K169A in the absence of agonists (PDB: 6UW6), and TRPV3-K169A in the presence of 100 μM of NASPM (this work), calculated by the MOLEonline server, shown as a colored surface representing electric potential (ChimeraX). Only two opposing subunits are shown for clarity. **B** Distances between constriction-forming diagonal sidechains at SF residue G638 and HBC residue I674 (Å). Only two opposing subunits are shown for clarity. **C** Water-accessible dimensions of K169A conduction pore in the presence of NASPM (green), compared to the WT closed (6UW4, blue), WT open (8V6N, yellow), and K169A open (6UW6, red), structures of TRPV3. Profiles are calculated with the program HOLE. Gray area represents an approximate location of the channel inner cavity. Major SF and HBC constrictions at G638 and I674 respectively, are labeled.

without affecting the voltage dependence of the blocking step, as well as markedly increased spermine permeation rates. TRPV1 and TRPV4 channels each contain only one 'ring' glutamate, and the striking similarity of WT TRPV1 and TRPV4 G_{rel}-V curves in the presence of 100 μM intracellular spermine[43] to those of the TRPV3-E682Q mutant (Table 1: $V^{mid}{}_1$ and $V^{mid}{}_2$), explains the difference in spermine block sensitivity between the channel subtypes. Interestingly, in BK channels a negatively charged 'ring' of 8 acidic residues, located at the entrance to the inner vestibule, mediates Mg^{2+} and PA block[33], hinting at a common mechanism of PA block in TRPs and potentially other cation channels that contain acidic residues at this location immediately below the inner cavity. At the same time, PA inhibition of TRPV1-4 appears to be distinct from previously reported block of the closely related TRPV5/6 channels by intracellular calmodulin[65,66] and PCHPDs[67] primarily due to its extremely high voltage sensitivity and relief at depolarizing potentials ([43], Fig. 2), both arising from the unique properties of PA molecules.

Previous extensive studies localized PA block of both potassium-selective inward rectifier channels[50,68] and non-selective AMPA[59] and kainate[69] receptors to the inner cavity and SF region of the pore. Given the presence of one negatively charged aspartate in the TRPV SF, we thus hypothesized that PA interaction may also occur in the SF region in TRPVs. However, neither TRPV3-L639M nor TRPV3-D641N mutants, the first mimicking the TRPV1 and TRPV4 SF 'GMGD' sequence, and the second neutralizing the aspartate residue in the SF (Fig. 1A), had any significant effect on spermine block (Fig. 2G), although addition of the D641N mutation did abolish the residual very weak block on the E679Q/E682Q background (Fig. 2H). This suggests a minor contribution of this location to controlling spermine permeation, consistent with previous reports of TRPV interaction with extra- as well as intracellular polyvalent cations[44,52,54].

Previous high-resolution structures of AMPA[59] and kainate[69] receptors visualized the bulky spermine analog NASPM and phylantotoxin PhTx-74 in the inner cavity and extending into the SF. In striking contrast to this, and to the binding of the weakly cationic hydrophobic TRPV3 pore blocker anesthetic dyclonine[63,70], we observe no NASPM-attributable density within the inner cavity or SF of TRPV3-K169A[58], even though this mutant channel spontaneously adopts an open and non-inactivating conformation in the absence of agonists, and our cryo-EM reconstruction was clear enough to visualize lipid-like densities decorating the channel. Moreover, the pore is closed, with tight constrictions at both the HBC and SF regions, such that the water-accessible surface profile between the HBC and the SF is almost identical to that of the WT channel in the completely closed state[56]. The remainder of the structure differs, however, with the pore-lining S6 maintaining a π-helical organization, as in both open (PDB: 6UW6) and closed (PDB: 6UW4), but not inactivated (PDB: 6UW9) states, and the CTD gating 'switch'[58] and ARD finger 5 loop as seen in the open structures. These latter features are consistent with the previously suggested TRPV3-K169A gating mechanism[56,58], as well as the heat-induced TRPV3 activation via 'conformational wave'[71], where the gating signal, ultimately resulting in the opening of the pore, is transferred from the α-helical CTD 'switch' via the finger 5 loop and linker domain rearrangements to the TRP helix and transmembrane domain.

The electrophysiological data strongly support channel block being the result of spermine or NASPM interaction with the E679 and E682 side chains that form the negative 'ring' immediately below the inner cavity: neutralization of either residue significantly reduces block, and block is essentially abolished in the double mutant (Figs. 2H, 3C). The quality of the cryo-EM density map for the E679 and E682 side chains (Fig. S1D, inset) was low, as it is not uncommon for acidic residues[72]. Tight binding of the blocker could theoretically have helped visualization of E679 and E682 residues, however, no specific NASPM density was observed in the region. These data suggest a quite dynamic interaction of polyamines with E679/E682 acidic sidechains, which may reflect the high flexibility of polyamine molecules. We propose that spermine interaction, in blocking the channel, promotes closure – or inhibits opening - of the pore above it, thereby excluding ions, including spermine, from entering the inner cavity, and explaining why the resolved cryo-EM structure is in a closed conformation in the presence of NASPM.

Based on both the electrophysiological and cryo-EM structural data, we propose a molecular model that qualitatively and quantitatively accounts for polyamine block of TRPV channels (Fig. 6). The model is similar to that we proposed previously[43] in assuming that bound polyamines block the channel, and that block can be relieved either by spermine unblocking to the cytoplasm or by permeating to the outside. In contrast to the previously proposed model, rather than a second blocking conformation arising from a distinct polyamine interaction reaction[43], we suggest that a second conformation is the result of the channel undergoing voltage-independent closure once polyamine is bound (Fig. 6A, B). Optimization of the model for spermine block of the WT channel involved voltage-dependence to spermine entry and exit, with the voltage-dependence potentially resulting from associated displacement of permeant ions towards the outside of the pore,

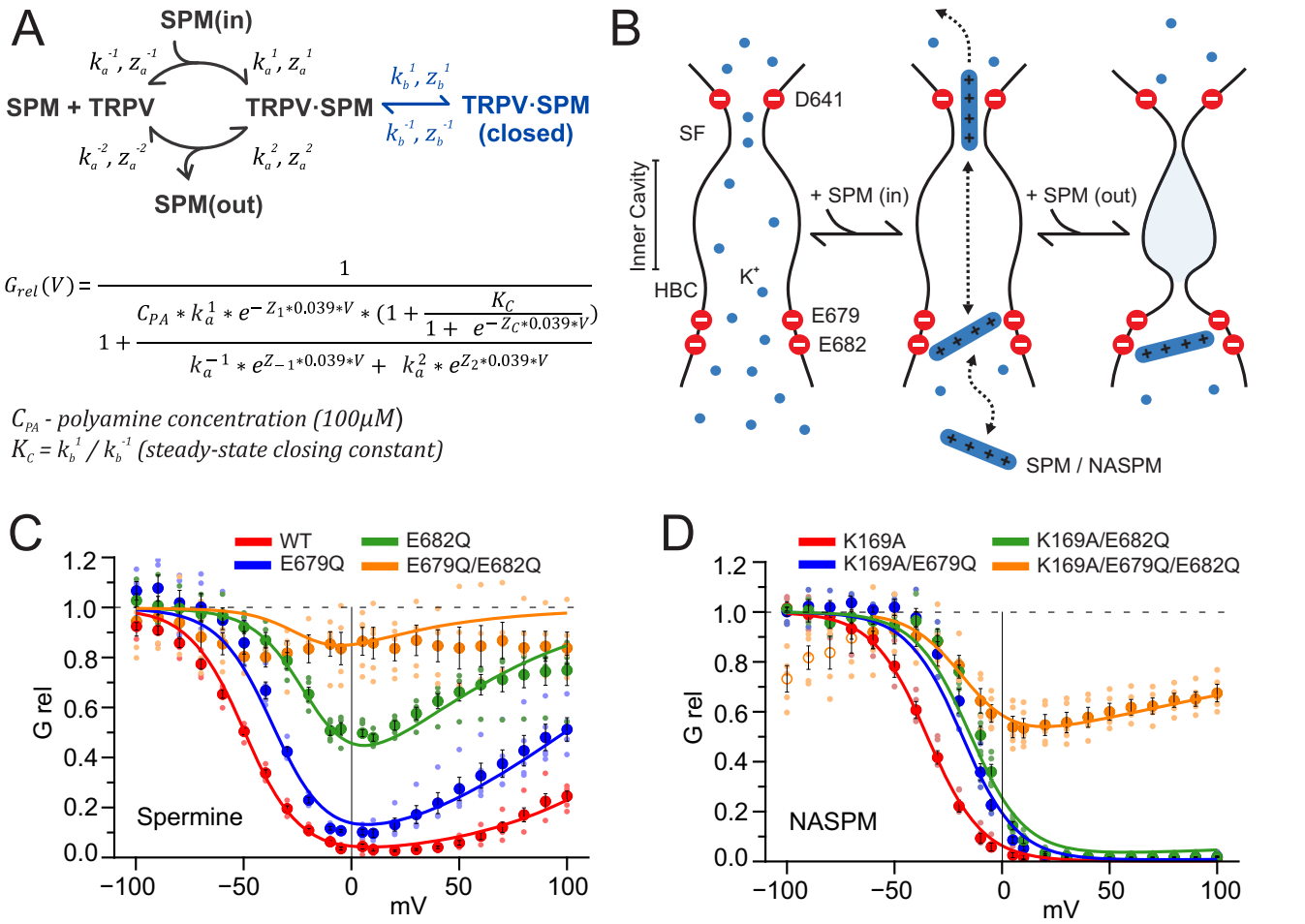

Fig. 6 | Proposed molecular mechanism of PA block of TRPV channels. **A** Modified kinetic model of TRPV3 inhibition by intracellular PAs. The model assumes that spermine interaction blocks the open channel. TRPV3-bound PA may either return to the cytoplasm, or permeate the channel and exit to the extracellular side, or force the channel to close. All transitions are reversible, however extracellular PA concentration is assumed to be zero. Relative conductance (G_{rel}, *Function 2*) is a function of intracellular PA and eight parameters (constants k_a^1, k_a^{-1}, k_a^2, K_C, and apparent charges associated with them), where $K_C = k_b^1 / k_b^{-1}$ and represents an equilibrium binding constant of PA bound to the closed TRPV channel. **B** Schematic representation of the hypothesized molecular mechanism of TRPV channel block by spermine. Key acidic residues (D641 above the SF and E679/E682 below the HBC) are labeled in red, spermine is presented as blue rods, and potassium ions are presented as blue beads. Open TRPV3 in the absence of spermine with both SF and HBC wide open, is permeable to potassium ions. Intracellular spermine (or NASPM) interacts with E679/E682 and blocks permeation. Spermine unblock can occur by return to the cytoplasm or by permeation to the outside. While interacting, spermine promotes channel closure. Model prediction of experimental data for WT and mutant TRPV3 in the presence of 100 μM intracellular spermine (**C**, n = 6 for WT, *n* = 5 for all mutants, ± SE) or NASPM (**D**, *n* = 5 for all, ± SE), data points from Figs. 2 and 3. Parameters were constrained as noted in Table 3. Data points labeled as empty circles (K169A/E679Q/E682Q) were excluded from analysis.

rather than the interaction site itself being within the field. Accordingly, the effects of individual E679 and E682 neutralizations were well predicted solely by reducing on-rates and increasing off-rates to the cytoplasm and permeation rates to the outside (Fig. 6A, C and Table 3) with no change in voltage-dependence, while the on-rate to off-rate ratios (K_a^1/K_a^{-1}, Table 3) reflected a highly dynamic interaction of polyamines with E679/E682 residues. The effect of the double E679Q/E682Q mutation was then well predicted by energetic summation of the effects of each individual mutation (Fig. 6C and Table 3).

The only essential change accounting for mutant channels was the interaction energy of 679/682 residues with polyamines. With variation of only 3 initial parameters (on-rate K_a^1, off-rate K_a^{-1}, and permeation rate K_a^2, Fig. 6A and Table 3), the model also accounts reasonably well for NASPM block, primarily by reducing the permeation rate. By similar energetically additive adjustments of entry and exit rates to those for spermine, NASPM block of E679 and E682 neutralization mutations is also accounted for (Fig. 6C, D and Table 3).

Structural and electrophysiological data support a model whereby cytoplasmic PA interaction with a ring of negatively charged residues at the entrance to the TRPV3 channel pore blocks permeation (and promotes channel closure), and block can be relieved by voltage-dependent permeation (Fig. 6B). A quantitative implementation of this model satisfactorily explains conductance-voltage relationships for block by spermine, or the bulky analog NASPM, of both wild type channels and mutations in which the critical 'ring' charges are neutralized. Increased understanding of the molecular mechanism of PA block of TRPV channels opens new avenues for investigation of novel voltage-dependent modulation of this important ion channel family.

Materials and methods

Channel constructs and drugs. All experiments were performed on the recombinant full-length human TRPV3[73,74] channel with a C-terminal EGFP tag, inserted into pPICZ-B vector and pV10 mammalian expression vector. Spermine, 1-Naphthylacetyl spermine trihydrochloride (NASPM), and 2-Aminoethoxydiphenylborate (2-APB) were purchased from Sigma. Point

mutations were introduced using QuikChange mutagenesis kit (Agilent). Sequences alignments (Fig. 1A) were made with Unipro UGENE suite[75].

Electrophysiology

HEK293 (Thermo Fischer Scientific) cells were transfected with 0.5 μg of human TRPV3-EGFP in pV10 vector per 35 mm Petri dish, using FuGENE6 (Promega), and were used for patch-clamp analysis of expressed channels within 24-48 hours. Patch-clamp experiments were performed on inside-out membrane patches, excised from cellular plasma membranes. Glass patch pipettes (Kimble Chase 2502) with ~2 MOhm resistance were produced with a Sutter P-96 puller (Sutter Instruments). The experiments were carried out in symmetric divalent-free solution (148 mM KCl, 1 mM EGTA, 1 mM K_2EDTA, 10 mM HEPES, pH 7.38). In experiments with the spontaneously active hTRPV3-K169A mutant, no agonist was used. In all experiments with WT hTRPV3, the agonist 2-APB at saturating concentration of 1 mM was applied to excised inside-out membrane patches via continuous bath perfusion. Relative conductance in the presence of spermine or NASPM was assessed by perfusion of the bath with the same solution, containing both 2-APB and respective polyamine (for WT TRPV3) or only polyamine (for TRPV3-K169A mutant) at 100 μM. Axopatch-200B patch-clamp amplifier (Axon Instruments) and Digidata 1320 digitizer (Axon Instruments) were used for data acquisition (3 kHz) and low-pass filtering (1 kHz).

Data processing and fitting

Data were further filtered and analyzed with pClamp 10.7 software suite (Molecular Devices). G_{rel}-V relationships for all TRPV3 mutants represent the average data (5–7 individual patches per data point ± S.E.) and were independently fit (Figs. 2, 3) in QtiPlot data analysis suite (Ion Vasilief, https://www.qtiplot.com):

(A). with the sum of two (ascending and descending) Boltzmann distributions (*Function 1*):

$$G_{rel}(V) = G_1^{\min} + \frac{(G_1^{\max} - G_1^{\min})}{1 + e^{Z_1 * 0.039 * (V_1^{mid} - V)}} + G_2^{\min} + \frac{(G_2^{\max} - G_2^{\min})}{1 + e^{Z_2 * 0.039 * (V - V_2^{mid})}}$$

where G^{min} and G^{max} are minimal and maximal normalized conductances (PA and agonist vs only agonist for WT TRPV3 and spontaneous activity in presence of PA vs spontaneous activity for TRPV3-K169A), Z_1 and Z_2 are gating charges, V^{mid} is a mid-point potential, and V is membrane potential, or were predicted (Fig. 6)

(B). with the suggested 2-state blocking model (*Function 2*):

$$G_{rel}(V) = \frac{1}{1 + \frac{C_{PA} * k_a^1 * e^{-Z_1 * 0.039 * V} * (1 + \frac{K_C}{1 + e^{-Z_C * 0.039 * V}})}{k_a^{-1} * e^{Z_{-1} * 0.039 * V} + k_a^2 * e^{Z_2 * 0.039 * V}}}$$

which implies one TRPV-PA interaction site, from which the PA may either dissociate back to the cytoplasm, or permeate the channel exiting to extracellular space, or drive the channel into the closed conformation (Fig. 6A). C_{PA} is intracellular polyamine (spermine or NASPM) concentration, while extracellular PA concentration is zero. $K_C = k_b^1/k_b^{-1}$ is the equilibrium association constant for PA in the closed channel state and its value was fixed at 6 (spermine fits) or 2 (NASPM fits). Z_1, Z_{-1}, Z_2, and Z_C are apparent charges associated with k_a^1, k_a^{-1}, k_a^2, and K_C respectively (Fig. 6A, B). For fitting all block experiments these charges were fixed: $Z_1 = 1$, $Z_{-1} = -1$, $Z_C = 0$ (no net charge transfer), and $Z_2 = 1.6$ or 1.2 for spermine and NASPM block respectively (Table 3). The ratio $k_a^2/k_a^{-1} = K_P$ (permeation constant, Table 3), represents the relative probability of PA traversing the channel vs going back to cytoplasm.

Graphics and modeling. Molecular structures (presented in Figs. 1, 5B) were plotted using University of Illinois VMD[76]. Water-accessible pore profiles (presented in Fig. 5C) were calculated with the RCSB.org alignment tool (rcsb.org/alignment)[77] and the program HOLE[78]. Pore electrostatic profiles (presented in Fig. 5A) were generated with MOLEonline server[79] and UCSF ChimeraX 1.7 suite[80].

Cryo-EM sample preparation

The TRPV3-K169A mutant was expressed, purified, and reconstituted into lipid nanodiscs following an established protocol[56]. The expression of TRPV3-K169A mutant was carried out in *Pichia pastoris*. The cells were disrupted by milling (Retsch MM400), followed by resuspension in lysis buffer containing 50 mM Tris-HCl pH 8.0, 150 mM NaCl, 2.5 μg/ml Leupeptin, 3 μg/ml Aprotinin, 1 μg/ml Pepstatin A, 1 mM Benzamidine, 200 μM phenylmethane sulphonylfluoride, 100 μg/ml 4-(2-Aminoethyl) benzenesulfonyl fluoride hydrochloride, and DNase I. The resuspended cells were then solubilized in 1% Lauryl Maltose Neopentyl Glycol (LMNG, Anatrace) for 2 hours. After centrifugation at 30,000 *g* for 30 minutes, the supernatant was collected and incubated with cobalt-charged resin (G-Biosciences) for 3 hours at 4°C. The resin was then washed with 30 mL of wash buffer containing 20 mM Tris-HCl, pH 8.0, 150 mM NaCl, 85 μM glyco-diosgenin (GDN, Anatrace), and 10 mM imidazole, followed by elution with buffer containing 20 mM Tris-HCl, pH 8.0, 150 mM NaCl, 85 μM GDN, and 200 mM imidazole.

The purified TRPV3-K169A mutant was then concentrated to ~20 μM and incubated with MSP2N2 and soybean polar lipid extract at a molar ratio of 1:0.5:50 for 10 minutes on ice. PreScission protease was then added to the mixture to remove the GFP-His_{10} tag. Bio-beads SM-2 resin (Bio-Rad) was added to the mixture to a final concentration of ~12.5% (v/v) and incubated overnight at 4°C. The resin was subsequently removed by centrifugation. Reconstituted proteins were further purified using a Superose 6 Increase 10/300 gel filtration column (GE Healthcare Life Sciences) equilibrated with 20 mM Tris-HCl pH 8.0 and 150 mM NaCl. Fractions were collected and concentrated to 1.5 mg/ml, and then incubated with 100 μM NASPM on ice for 20 min before freezing.

A volume of 3.5 μl protein sample was applied to glow-discharged Quantifoil R1.2/1.3 copper grids (Q350CR1.3, Electron Microscopy Sciences). The grids were blotted for 2 s after waiting for 20 s at 4 °C and 100% humidity, and then plunged into liquid ethane using the FEI Vitrobot Mark IV (FEI). The grids were then imaged under a Glacios Cryo-TEM operating at 200 kV with a Falcon IV detector (ThermoFisher Scientific) at a magnification of 120 k, with a defocus range from −0.8 to -2.4 μm and pixel size of 1.2 Å. The total accumulated dose was 44.1 $e^-/Å^2$ (Table 4).

Cryo-EM data collection and processing

3,749 raw movies were imported into cryoSPARC V3.4.0[81] and subjected to patch motion correction and patch CTF estimation. After discarding low-quality images, 3744 images were used for blob and template-based particle picking. These particles were then subjected to 2D classification. High-quality particles were selected to generate initial 3D models for subsequent heterogeneous refinement. To further improve the map quality, a total of 266,529 final particles were subjected to non-uniform refinement, local refinement, and global CTF refinement with imposed C4 symmetry (Fig. S1).

Model building and visualization

To build the model of TRPV3-K169A with NASPM, wild-type TRPV3 (PDB: 6UW4) and TRPV3-K169A (PDB: 6UW6) models were used as initial templates. After adjusting the initial models with rigid body fit and real-space refinement in COOT 0.9[82], the model was further refined against the sharpened map by real-space refinement in PHENIX 1.20.1[83]. Model evaluation was performed using MolProbity[84]. Figure images were generated with UCSF ChimeraX 1.7 suite[80].

Statistics and reproducibility

Each data point in Figs. 2, 3, and 6 represents a measurement obtained from individual patches, all pulled from different cells. The mean values and standard errors were calculated from the data obtained from at least 5 individual patches (n = 5 - 7, specified in figure captions). Results in the

Table 4 | Cryo-EM data collection, refinement, and validation statistics

	TRPV3-K169A in nanodiscs with NASPM (EMD-44645) (PDB 9BKU)
Data collection and processing	
Magnification	120k
Voltage (kV)	200
Electron exposure ($e^-/Å^2$)	44.1
Defocus range (μm)	−0.8 to −2.4
Pixel size (Å)	1.2
Symmetry imposed	C4
Initial particle images (no.)	1,864,667
Final particle images (no.)	266,529
Map resolution (Å)	3.4
FSC threshold	0.143
Map resolution range (Å)	2.5–4.5
Refinement	
Initial model used (PDB code)	6UW6
Model resolution (Å)	3.6
FSC threshold	0.5
Map sharpening *B* factor ($Å^2$)	−162.7
Model composition	
Nonhydrogen atoms	17,504
Protein residues	2,352
Ligands	36
B factors ($Å^2$)	
Protein	60.52
Ligand	56.37
R.m.s. deviations	
Bond lengths (Å)	0.002
Bond angles (°)	0.425
Validation	
MolProbity score	1.55
Clash score	6.01
Poor rotamers (%)	0
Ramachandran plot	
Favored (%)	96.54
Allowed (%)	3.46
Disallowed (%)	0

figures are reported as mean values along with individual data points, SE error bars, and fitted curves.

Reporting summary

Further information on research design is available in the Nature Portfolio Reporting Summary linked to this article.

Data availability

Data supporting the findings of this manuscript are available from the corresponding author upon reasonable request. Electrophysiological data have been deposited in a Zenodo repository [https://doi.org/10.5281/zenodo.15133465]. The TRPV3-K169A with NASPM model was deposited in the Protein Data Bank under accession code 9BKU. Maps were deposited in the Electron Microscopy Data Bank with accession code EMD-44645.

Received: 4 November 2024; Accepted: 17 April 2025;
Published online: 10 May 2025

References

1. Igarashi, K. & Kashiwagi, K. The functional role of polyamines in eukaryotic cells. *Int J. Biochem. Cell Biol.* **107**, 104–115 (2019).
2. Bekebrede, A. F. et al. The molecular and physiological effects of protein-derived polyamines in the intestine. *Nutrients* **12**. (2020).
3. Dever, T. E. & Ivanov, I. P. Roles of polyamines in translation. *J. Biol. Chem.* **293**, 18719–18729 (2018).
4. Malpica-Nieves, C. J. et al. The involvement of polyamine uptake and synthesis pathways in the proliferation of neonatal astrocytes. *Amino Acids* **52**, 1169–1180 (2020).
5. Nakamura, A. et al. Symbiotic polyamine metabolism regulates epithelial proliferation and macrophage differentiation in the colon. *Nat. Commun.* **12**, 2105 (2021).
6. Chamoto, K. et al. Spermidine - an old molecule with a new age-defying immune function. *Trends Cell Biol*. (2023).
7. Chia, T. Y., Zolp, A. & Miska, J. Polyamine immunometabolism: central regulators of inflammation, cancer and autoimmunity. *Cells* **11**. (2022).
8. Babbar, N., Murray-Stewart, T. & Casero, R. A. Jr Inflammation and polyamine catabolism: the good, the bad and the ugly. *Biochem. Soc. Trans.* **35**, 300–304 (2007).
9. Cruz-Pulido, Y. E. & Mounce, B. C. Good cop, bad cop: Polyamines play both sides in host immunity and viral replication. *Semin. Cell Dev. Biol.* **146**, 70–79 (2023).
10. Malta-Santos, H. et al. Differential expression of polyamine biosynthetic pathways in skin lesions and in plasma reveals distinct profiles in diffuse cutaneous leishmaniasis. *Sci. Rep.* **10**, 10543 (2020).
11. Shao, J. et al. Versatile roles of polyamines in improving abiotic stress tolerance of plants. *Front. Plant Sci.* **13**, 1003155 (2022).
12. Lewandowski, N. M. et al. Polyamine pathway contributes to the pathogenesis of Parkinson disease. *Proc. Natl. Acad. Sci. USA* **107**, 16970–16975 (2010).
13. Minois, N. Molecular basis of the 'anti-aging' effect of spermidine and other natural polyamines - a mini-review. *Gerontology* **60**, 319–326 (2014).
14. Polis, B., Karasik, D. & Samson, A. O. Alzheimer's disease as a chronic maladaptive polyamine stress response. *Aging* **13**, 10770–10795 (2021).
15. Saiki, S. et al. A metabolic profile of polyamines in parkinson disease: A promising biomarker. *Ann. Neurol.* **86**, 251–263 (2019).
16. Li, J. et al. Polyamines and related signaling pathways in cancer. *Cancer Cell Int.* **20**, 539 (2020).
17. Holbert, C. E. et al. Polyamines in cancer: integrating organismal metabolism and antitumour immunity. *Nat. Rev. Cancer* **22**, 467–480 (2022).
18. Arruabarrena-Aristorena, A., Zabala-Letona, A. & Carracedo, A. Oil for the cancer engine: The cross-talk between oncogenic signaling and polyamine metabolism. *Sci. Adv.* **4**, eaar2606 (2018).
19. Bachmann, A. S. et al. Bachmann-Bupp syndrome and treatment. *Dev. Med. Child Neurol*. (2023).
20. Cason, A. L. et al. X-linked spermine synthase gene (SMS) defect: the first polyamine deficiency syndrome. *Eur. J. Hum. Genet.* **11**, 937–944 (2003).
21. Schroeder, S. et al. Dietary spermidine improves cognitive function. *Cell Rep.* **35**, 108985 (2021).
22. Ghosh, I. et al. Spermidine, an autophagy inducer, as a therapeutic strategy in neurological disorders. *Neuropeptides* **83**, 102083 (2020).
23. Wirth, M. et al. The effect of spermidine on memory performance in older adults at risk for dementia: A randomized controlled trial. *Cortex* **109**, 181–188 (2018).
24. Bui, T. I. et al. Probiotic induced synthesis of microbiota polyamine as a nutraceutical for metabolic syndrome and obesity-related type 2 diabetes. *Front. Endocrinol.* **13**, 1094258 (2022).

25. Niechcial, A. et al. Spermidine ameliorates colitis via induction of anti-inflammatory macrophages and prevention of intestinal dysbiosis. *J. Crohns Colitis* **17**, 1489–1503 (2023).
26. Casero, R. A. Jr, Murray Stewart, T. & Pegg, A. E. Polyamine metabolism and cancer: treatments, challenges and opportunities. *Nat. Rev. Cancer* **18**, 681–695 (2018).
27. Chin, A. et al. Polyamine depletion strategies in cancer: remodeling the tumor immune microenvironment to enhance anti-tumor responses. *Med. Sci*. **10**, (2022).
28. Gitto, S. B. et al. Difluoromethylornithine combined with a polyamine transport inhibitor is effective against Gemcitabine resistant pancreatic cancer. *Mol. Pharm.* **15**, 369–376 (2018).
29. Sholler, G. L. S. et al. Maintenance DFMO increases survival in high risk neuroblastoma. *Sci. Rep.* **8**, 14445 (2018).
30. Lopatin, A. N., Makhina, E. N. & Nichols, C. G. Potassium channel block by cytoplasmic polyamines as the mechanism of intrinsic rectification. *Nature* **372**, 366–369 (1994).
31. Nichols, C. G. & Lee, S. J. Polyamines and potassium channels: A 25-year romance. *J. Biol. Chem.* **293**, 18779–18788 (2018).
32. Kucheryavykh, Y. V. et al. Polyamine permeation and rectification of Kir4.1 channels. *Channels* **1**, 172–178 (2007).
33. Zhang, Y. et al. Ring of negative charge in BK channels facilitates block by intracellular Mg2+ and polyamines through electrostatics. *J. Gen. Physiol.* **128**, 185–202 (2006).
34. Huang, C. J. & Moczydlowski, E. Cytoplasmic polyamines as permeant blockers and modulators of the voltage-gated sodium channel. *Biophys. J.* **80**, 1262–1279 (2001).
35. Bowie, D. Polyamine-mediated channel block of ionotropic glutamate receptors and its regulation by auxiliary proteins. *J. Biol. Chem.* **293**, 18789–18802 (2018).
36. Bowie, D., Lange, G. D. & Mayer, M. L. Activity-dependent modulation of glutamate receptors by polyamines. *J. Neurosci.* **18**, 8175–8185 (1998).
37. Guo, D. & Lu, Z. Mechanism of cGMP-gated channel block by intracellular polyamines. *J. Gen. Physiol.* **115**, 783–798 (2000).
38. Lu, Z. & Ding, L. Blockade of a retinal cGMP-gated channel by polyamines. *J. Gen. Physiol.* **113**, 35–43 (1999).
39. Kim, J. et al. Analysis of interaction between intracellular spermine and transient receptor potential canonical 4 channel: multiple candidate sites of negatively charged amino acids for the inward rectification of transient receptor potential canonical 4. *Korean J. Physiol. Pharm.* **24**, 101–110 (2020).
40. Kim, J. et al. Intracellular spermine blocks TRPC4 channel via electrostatic interaction with C-terminal negative amino acids. *Pflug. Arch.* **468**, 551–561 (2016).
41. Nilius, B. et al. Intracellular nucleotides and polyamines inhibit the Ca2+-activated cation channel TRPM4b. *Pflug. Arch.* **448**, 70–75 (2004).
42. Zhelay, T. et al. Depletion of plasma membrane-associated phosphoinositides mimics inhibition of TRPM7 channels by cytosolic Mg(2+), spermine, and pH. *J. Biol. Chem.* **293**, 18151–18167 (2018).
43. Maksaev, G., Yuan, P. & Nichols, C. G. Blockade of TRPV channels by intracellular spermine. *J. Gen. Physiol.***155**, (2023).
44. Ahern, G. P., Wang, X. & Miyares, R. L. Polyamines are potent ligands for the capsaicin receptor TRPV1. *J. Biol. Chem.* **281**, 8991–8995 (2006).
45. Zubcevic, L. et al. Conformational plasticity in the selectivity filter of the TRPV2 ion channel. *Nat. Struct. Mol. Biol.* **25**, 405–415 (2018).
46. Yuan, P. Structural biology of thermoTRPV channels. *Cell Calcium* **84**, 102106 (2019).
47. Deng, Z. et al. Cryo-EM and X-ray structures of TRPV4 reveal insight into ion permeation and gating mechanisms. *Nat. Struct. Mol. Biol.* **25**, 252–260 (2018).
48. Yang, F. et al. An Unorthodox Mechanism Underlying Voltage Sensitivity of TRPV1 Ion Channel. *Adv. Sci.* **7**, 2000575 (2020).
49. White, J. P. et al. TRPV4: Molecular Conductor of a Diverse Orchestra. *Physiol. Rev.* **96**, 911–973 (2016).
50. Jogini, V., Jensen, M. O. & Shaw, D. E. Gating and modulation of an inward-rectifier potassium channel. *J. Gen. Physiol.* **155**, (2023).
51. Lopatin, A. N., Makhina, E. N. & Nichols, C. G. The mechanism of inward rectification of potassium channels: “long-pore plugging” by cytoplasmic polyamines. *J. Gen. Physiol.* **106**, 923–955 (1995).
52. Tousova, K. et al. Gadolinium activates and sensitizes the vanilloid receptor TRPV1 through the external protonation sites. *Mol. Cell Neurosci.* **30**, 207–217 (2005).
53. Wang, H. et al. Mechanisms of proton inhibition and sensitization of the cation channel TRPV3. *J. Gen. Physiol.***153**, (2021).
54. Luo, J. et al. Tonic inhibition of TRPV3 by Mg2+ in mouse epidermal keratinocytes. *J. Invest. Dermatol.* **132**, 2158–2165 (2012).
55. Nadezhdin, K. D. et al. TRPV3 activation by different agonists accompanied by lipid dissociation from the vanilloid site. *Sci. Adv.* **10**, eadn2453 (2024).
56. Deng, Z. et al. Gating of human TRPV3 in a lipid bilayer. *Nat. Struct. Mol. Biol.* **27**, 635–644 (2020).
57. Phelps, C. B. et al. Differential regulation of TRPV1, TRPV3, and TRPV4 sensitivity through a conserved binding site on the ankyrin repeat domain. *J. Biol. Chem.* **285**, 731–740 (2010).
58. Zubcevic, L. et al. Regulatory switch at the cytoplasmic interface controls TRPV channel gating. *Elife* **8**, (2019).
59. Twomey, E. C. et al. Mechanisms of channel block in calcium-permeable AMPA receptors. *Neuron* **99**, 956–968 e4 (2018).
60. Zubcevic, L. et al. Conformational ensemble of the human TRPV3 ion channel. *Nat. Commun.* **9**, 4773 (2018).
61. Fan, J. et al. Structural basis of TRPV3 inhibition by an antagonist. *Nat. Chem. Biol.* **19**, 81–90 (2023).
62. Neuberger, A. et al. Structural mechanism of TRPV3 channel inhibition by the plant-derived coumarin osthole. *EMBO Rep.* **22**, e53233 (2021).
63. Neuberger, A., Nadezhdin, K. D. & Sobolevsky, A. I. Structural mechanism of TRPV3 channel inhibition by the anesthetic dyclonine. *Nat. Commun.* **13**, 2795 (2022).
64. Singh, A. K., McGoldrick, L. L. & Sobolevsky, A. I. Structure and gating mechanism of the transient receptor potential channel TRPV3. *Nat. Struct. Mol. Biol.* **25**, 805–813 (2018).
65. Hughes, T. E. T. et al. Structural insights on TRPV5 gating by endogenous modulators. *Nat. Commun.* **9**, 4198 (2018).
66. Singh, A. K. et al. Mechanism of calmodulin inactivation of the calcium-selective TRP channel TRPV6. *Sci. Adv.* **4**, eaau6088 (2018).
67. Bhardwaj, R. et al. Inactivation-mimicking block of the epithelial calcium channel TRPV6. *Sci. Adv.* **6**. (2020).
68. Lee, S. J. & Nichols, C. G. Seeing spermine blocking of K+ ion movement through inward rectifier Kir2.2 channels. *J. Gen. Physiol.* **155**, (2023).
69. Gangwar, S. P. et al. Trapping of spermine, Kukoamine A, and polyamine toxin blockers in GluK2 kainate receptor channels. *Nat. Commun.* **15**, 10257 (2024).
70. Liu, Q. et al. Therapeutic inhibition of keratinocyte TRPV3 sensory channel by local anesthetic dyclonine. *Elife* **10**. (2021).
71. Nadezhdin, K. D. et al. Structural mechanism of heat-induced opening of a temperature-sensitive TRP channel. *Nat. Struct. Mol. Biol.* **28**, 564–572 (2021).
72. Marques, M. A., Purdy, M. D. & Yeager, M. CryoEM maps are full of potential. *Curr. Opin. Struct. Biol.* **58**, 214–223 (2019).
73. Peier, A. M. et al. A heat-sensitive TRP channel expressed in keratinocytes. *Science* **296**, 2046–2049 (2002).
74. Smith, G. D. et al. TRPV3 is a temperature-sensitive vanilloid receptor-like protein. *Nature* **418**, 186–190 (2002).
75. Okonechnikov, K. et al. Unipro UGENE: a unified bioinformatics toolkit. *Bioinformatics* **28**, 1166–1167 (2012).
76. Humphrey, W., Dalke, A. & Schulten, K. VMD: visual molecular dynamics. *J. Mol. Graph* **14**, 33–38 (1996).

77. Bittrich, S. et al. RCSB protein Data Bank: exploring protein 3D similarities via comprehensive structural alignments. *Bioinformatics* **40**. (2024).
78. Smart, O. S. et al. HOLE: a program for the analysis of the pore dimensions of ion channel structural models. *J. Mol. Graph* **14**, 354–360 (1996).
79. Pravda, L. et al. MOLEonline: a web-based tool for analyzing channels, tunnels and pores (2018 update). *Nucleic Acids Res* **46**, W368–W373 (2018).
80. Pettersen, E. F. et al. UCSF ChimeraX: Structure visualization for researchers, educators, and developers. *Protein Sci.* **30**, 70–82 (2021).
81. Punjani, A., Rubinstein, J. L., Fleet, D. J. & Brubaker, M. A. cryoSPARC: algorithms for rapid unsupervised cryo-EM structure determination. *Nat. Methods* **14**, 290–296 (2017).
82. Emsley, P., Lohkamp, B., Scott, W. G. & Cowtan, K. Features and development of Coot. *Acta. Crystallogr. D Biol. Crystallogr.* **66**, 486–501 (2010).
83. Adams, P. D. et al. PHENIX: a comprehensive Python-based system for macromolecular structure solution. *Acta. Crystallogr. D Biol. Crystallogr.* **66**, 213–221 (2010).
84. Chen, V. B. et al. MolProbity: all-atom structure validation for macromolecular crystallography. *Acta. Crystallogr. D Biol. Crystallogr.* **66**, 12–21 (2010).

Author contributions

G.M., P.Y., and C.G.N. conceived the project. G.M. carried out mutagenesis, molecular biology manipulations, and electrophysiological experiments and supervised the project. J.Z. performed biochemical preparations, cryo-EM experiments, structure determination, and analysis. J.Z., G.M., P.Y., and C.G.N. analyzed the experimental data. G.M. wrote the manuscript, which was edited by the other authors.

Competing interests

The authors declare no competing interests.

Additional information

Supplementary information The online version contains supplementary material available at https://doi.org/10.1038/s42003-025-08103-x.

Correspondence and requests for materials should be addressed to Grigory Maksaev.

Peer review information *Communications Biology* thanks Makoto Tominaga, Alexander Sobolevsky, and the other anonymous reviewer(s) for their contribution to the peer review of this work. Primary Handling Editors: Laura Rodríguez Pérez.